The Noise of Membrane Capacitance Measurements in the Whole-Cell Recording Configuration

Peng Chen* and Kevin D. Gillis†

Departments of *Electrical Engineering; †Physiology and *Dalton Cardiovascular Research Center, University of Missouri–Columbia, Research Park, Columbia, Missouri 65211 USA

ABSTRACT High-resolution measurement of membrane capacitance in the whole-cell-recording configuration can be used to detect small changes in membrane surface area that accompany exocytosis and endocytosis. We have investigated the noise of membrane capacitance measurements to determine the fundamental limits of resolution in actual cells in the whole-cell mode. Two previously overlooked sources of noise are particularly evident at low frequencies. The first noise source is accompanied by a correlation between capacitance estimates, whereas the second noise source is due to "1/*f*-like" current noise. An analytic expression that summarizes the noise from thermal and 1/*f* sources is derived, which agrees with experimental measurements from actual cells over a large frequency range. Our results demonstrate that the optimal frequencies for capacitance measurements are higher than previously believed. Finally, we demonstrate that the capacitance noise at high frequencies can be reduced by compensating for the voltage drop of the sine wave across the series resistance.

INTRODUCTION

Patch-clamp techniques have not only revolutionized the study of ion channels, but have also been applied to study exocytosis and endocytosis from single cells with unprecedented resolution (see Gillis, 1995 for a review). Electrical measurements of the capacitance of the cell membrane can be used to detect exocytosis because changes in membrane surface area accompany fusion of secretory vesicles with the plasma membrane. The fusion of individual vesicles, just like the opening of single ion channels, can most easily be resolved in recordings from membrane patches. With careful attention to noise originating from the recording instrumentation, capacitance noise of 25 aF, can be achieved in on-cell recordings (Lollike et al., 1995). However, capacitance measurements in the whole-cell configuration are most popular for studying the regulation of exocytosis. In the whole-cell mode, it is often the thermal (Johnson) noise of the equivalent circuit of the cell, rather than the recording instrumentation, which limits the resolution of capacitance measurements at high frequencies.

In a previous study, we derived an approximate expression for the variance of capacitance estimates that originates from thermal current noise (Gillis, 1995), however, experimental measurements from a model circuit exhibited higher-than-predicted noise at low frequencies. We have resolved this discrepancy in the present study by deriving a more exact expression for capacitance noise and demonstrating that the "excess" noise is associated with a correlation among capacitance estimates that was neglected in the previous study. In addition, we show how 1/*f*-like current noise increases the capacitance noise in recordings from actual cells at low frequencies. Finally, we demonstrate how noise at high frequencies can be reduced by the use of series resistance compensation implemented in hardware or software.

Received for publication 7 December 1999 and in final form 5 July 2000.

Address reprint requests to Kevin D. Gillis, Dalton Cardiovascular Research Center, University of Missouri–Columbia, Research Park, Columbia, MO 65211. Tel.: 573-884-8805; Fax: 573-884-4232; E-mail: gillisk@missouri.edu.

0006-3495/00/10/2162/09 $2.00

MATERIALS AND METHODS

Cell preparation and solutions

Bovine adrenal chromaffin cells were prepared as previously described (Zhou and Neher, 1993) and used between 1 and 4 days after isolation. NIH3T3 cells were a gift from Dr. Tzyh-Chang Hwang, and were cultured at 37°C in Dulbecco's modified Eagle's medium supplemented with 2 mM glutamine and 10% calf serum. Cells were passaged and plated out on glass coverslips for use on the following day. Experiments were performed at room temperature (22–24°C). All chemicals were purchased from Sigma (St. Louis, MO). The bath solution contained (in mM): 140 NaCl, 5.5 KCl, 11 $MgCl_2$, 10 glucose, and 10 Na-HEPES (pH 7.2). In the experiments depicted in Fig. 5 *A*, 50 μM $CdCl_2$ and 10 μM tetrodotoxin were added to the bath. The pipette contained 150 Cs-glutamate, 3 $MgCl_2$, 2 Na_2ATP, 0.5 EGTA and 10 Cs-HEPES (pH 7.2). In some experiments, *N*-methyl glucamine was used instead of Cs.

Electrophysiology and data analysis

Recording pipettes were pulled from Kimax glass, coated with wax and fire polished. Pipette resistance ranged between 1.5 and 4 MΩ. An EPC-9 patch-clamp amplifier was used together with PULSE software (HEKA Elektronik, Lambrecht, Germany) for data acquisition.

Capacitance measurements were performed using the "sine + dc" (Lindau–Neher) method implemented in PULSE software (Gillis, 2000; Gillis, 1995; Lindau and Neher, 1988; Pusch and Neher, 1988). The reversal potential was assumed to be 0 mV and the holding potential was −70 mV except as indicated. The amplitude of the stimulus sinusoid was 25 mV (50 mV peak-to-peak), except as indicated, and the frequency ranged between 200 Hz and 5 kHz. The 10-kHz Bessel filter of the EPC-9 was used to low-pass filter the current, and the sampling rate was fixed at 50 ksamples/s. The current power spectral density was obtained using the Fast Fourier Transform feature of PULSE, which uses a sample interval of 20 μs and 1024 points per sweep. The results of 1000 or more sweeps were averaged to obtain the power spectral density. Capacitance noise was

calculated as the standard deviation of sweeps 10 s in duration. Sweeps with exhibited slow changes in capacitance were excluded from analysis. Curve fitting and data analysis were performed using macros written in Igor (Wavemetrics, Inc., Lake Oswego, OR).

RESULTS

Noise of C_m measurements due to Johnson (thermal) noise

The equivalent circuit of a cell in the whole-cell-recording configuration is depicted in Fig. 1. Resistors are energy-dissipating devices and thus exhibit fluctuations of thermal origin. The power spectral density of the current fluctuations of a circuit originating from thermal noise is given by

$$S_I(f) = 4kT \cdot \mathrm{Real}\{Y(f)\} \quad 0 < f < \infty, \tag{1}$$

where k is the Boltzmann constant, T is absolute temperature and $Y(f)$ is the admittance of the circuit. For the equivalent circuit depicted in Fig. 1, the admittance is given by

$$Y(\omega) = \frac{(1 + j\omega R_m C_m)}{R_t(1 + j\omega R_p C_m)}, \tag{2}$$

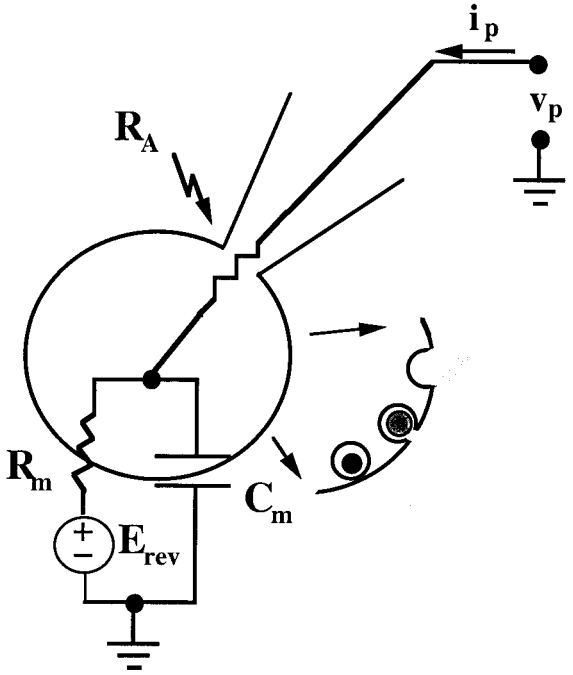

FIGURE 1 The equivalent circuit of a cell in the whole-cell recording configuration. R_A is the access resistance between the pipette and the cell interior, R_m is the membrane resistance, and C_m is the membrane capacitance. v_p is the voltage between the pipette and bath ground, whereas i_p is the current into the pipette. The capacitance between the pipette and bath ground is neglected because the current through this pathway is electronically subtracted using pipette capacitance compensation circuitry of the patch-clamp amplifier.

where $R_t = R_A + R_m R_p = R_A R_m/(R_A + R_m)$, $\omega = 2\pi f$, and $j = (-1)^{1/2}$. The real part of the admittance is therefore given by

$$\mathrm{Real}\{Y(\omega)\} = \frac{1 + \omega^2 R_m R_p C_m^2}{R_t(1 + \omega^2 R_p^2 C_m^2)}. \tag{3}$$

The power spectral density leads to a current variance, given by

$$\sigma_I^2 = \int_0^\infty |H(f)|^2 S_I(f)\, df, \tag{4}$$

where $H(f)$ is the transfer function of the measuring apparatus. $H(f)$ can be thought of as a "weighting function" that describes the filtering of the various frequency components that make up the current signal.

The fluctuations in current described by Eq. 1 lead to fluctuations in estimates of C_m. To quantify the C_m noise, we first need to consider how current is processed to produce C_m estimates. Typically, a sine wave voltage stimulus is applied and the resulting sinusoidal current is used to calculate either the actual admittance or a relative change in admittance. The admittance estimates are then processed to produce estimates of C_m (see Gillis, 1995, 2000 for details).

Estimates of the real and imaginary components of the admittance are obtained by processing the current (i_p) with a phase-sensitive detector (lock-in amplifier) implemented either in hardware or software. The operation of a software phase-sensitive detector can be mathematically described by the following equations:

$$\mathrm{Real}\{\hat{Y}(f_c)\} = \frac{2}{UmT_c}\int_0^{mT_c} i_p(t)\cos(\omega_c t)\, dt,$$

$$\mathrm{Imag}\{\hat{Y}(f_c)\} = \frac{2}{UmT_c}\int_0^{mT_c} i_p(t)\sin(\omega_c t)\, dt, \tag{5}$$

where U is the amplitude of the applied voltage stimulus of frequency f_c, T_c is the period of the sinusoid ($= 1/f_c$), and m is the number of cycles that are used to produce a single estimate. By analogy with Eq. 4, the noise of an admittance estimate (either the real part or the imaginary part) is then given by

$$\sigma_{\hat{Y}}^2 = \frac{1}{U^2}\int_0^\infty |H_{psd}(f)|^2 S_I(f)\, df, \tag{6}$$

where H_{psd} is the transfer function of the software phase-sensitive detector given by (Gillis, 1995)

$$|H_{psd}(f)| = \left|\frac{\sin[\pi m(f - f_c)/f_c]}{\pi m(f - f_c)/f_c}\right|. \tag{7}$$

Figure 2 plots H_{psd} for m values of 1 (*dark solid line*) and 10 (*light solid line*). Note that the software phase-sensitive detector acts as a band-pass filter centered at the stimulus frequency (f_c). As m increases, the width of the pass band decreases, making the phase-sensitive detector more selective for frequencies near f_c. However, a larger value of m also means that estimates of C_m are generated at a slower rate (f_c/m). Hardware lock-in amplifiers also act as band-pass filters, with a bandwidth determined by the time constant(s) of the RC filters at the output of the device. Longer time constants result in narrower pass bands and more highly filtered C_m estimates. Fig. 2 also plots H_{psd} for a hardware lock-in amplifier with a single time constant (*dashed line*, $\tau = 5/f_c$).

Next, we need to relate the noise of admittance measurements to the noise of the resulting capacitance estimates. For a high signal-to-noise ratio, a linear approximation can be made (Gillis, 1995),

$$\sigma_{\hat{C}} = \frac{\sigma_{\hat{Y}}}{|\partial Y/\partial C_m|}, \tag{8}$$

where $|\partial Y/\partial C_m|$ is given by

$$\left|\frac{\partial Y}{\partial C_m}\right| = \frac{\omega_c R_m^2}{R_t^2(1 + \omega_c^2 R_p^2 C_m^2)}. \tag{9}$$

Therefore, to obtain an analytic solution for C_m noise, we need only to solve Eq. 6. In Gillis (1995), the solution to Eq. 6 was approximated by

$$\sigma_{\hat{Y}}^2 \approx \frac{1}{U^2} S_I(f_c) B_N \equiv \sigma_{\hat{Y},approx}^2, \tag{10}$$

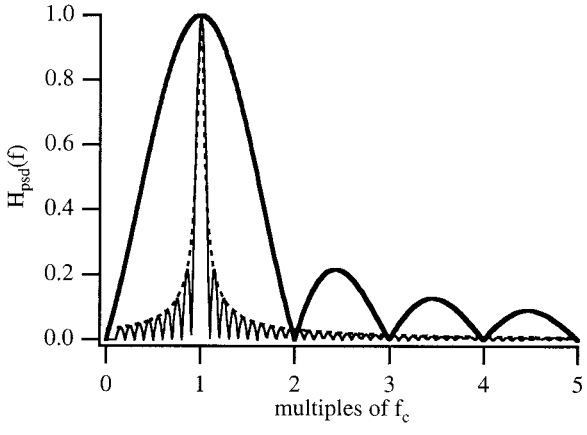

FIGURE 2 The phase-sensitive detector (lock-in amplifier) acts as a band-pass filter. The amplitude of the transfer function of the phase-sensitive detector is plotted versus frequency. The darker solid line is for a software phase-sensitive detector with m (the number of sine wave cycles that are used for the calculation) = 1 (see Eq. 7). The lighter line is for a software phase-sensitive detector with m = 10. Note that the phase-sensitive detector becomes more selective for frequencies near that of the stimulus (f_c) as m increases. The dashed line depicts the transfer function for a hardware lock-in amplifier with a single time constant filter, $\tau = 5/f_c$.

where B_N is the noise bandwidth of the phase-sensitive detector. For the case of the software phase-sensitive detector described above, B_N is given by

$$B_N \equiv \int_0^\infty |H_{psd}(f)|^2 \, df \approx \frac{f_c}{m}. \tag{11}$$

The approximation in Eq. 10 assumes that the phase-sensitive detector only measures the stimulus frequency (f_c), i.e., $H_{psd} = 0$ for frequencies other than f_c. Consideration of Eq. 7 and Fig. 2 reveals that the approximation becomes exact in the limit as m approaches infinity. Combining Eqs. 8–11 results in the approximate expression for C_m variance originating from thermal fluctuations given by Gillis (1995) and reproduced here:

$$\sigma_{\hat{C},approx}^2 \approx \frac{4kTf_c(1 + \omega_c^2 R_m R_p C_m^2)(1 + \omega_c^2 R_p^2 C_m^2) R_t^3}{m\omega_c^2 U^2 R_m^4}. \tag{12}$$

Figure 3 *A* presents experimental measurements of capacitance noise as a function of stimulus frequency for a model circuit (*squares*). The measurements were made with a constant bandwidth of 100 Hz, i.e., m was adjusted so that the ratio f_c/m remains constant at 100 Hz. The dashed line indicates the noise predicted from Eq. 12. Note that the agreement is quite good at high frequencies. However, the measured noise exceeds the predicted value at low frequencies. To better understand the noise at low frequencies, we have obtained an exact solution to Eq. 6 for the case of the software phase-sensitive detector (derived in the appendix):

$$\sigma_{\hat{Y}}^2 = \sigma_{\hat{Y},approx}^2 \left[1 + \frac{2f_c R_m^2 C_m (1 - \exp[-mT_c/R_p C_m])}{mR_t(1 + \omega_c^2 R_m R_p C_m^2)(1 + \omega_c^2 R_p^2 C_m^2)}\right]. \tag{13}$$

The term in braces in Eq. 13 can be considered a correction factor. Because the variance of capacitance estimates is linearly related to the variance of admittance estimates (Eq. 8), Eq. 12 can be multiplied by the correction factor of Eq. 13 to yield

$$\sigma_{\hat{C}}^2 = \frac{4kTf_c(1 + \omega_c^2 R_m R_p C_m^2)(1 + \omega_c^2 R_p^2 C_m^2) R_t^3}{m\omega_c^2 U^2 R_m^4} \times \left[1 + \frac{2f_c R_m^2 C_m (1 - \exp[-mT_c/R_p C_m])}{mR_t(1 + \omega_c^2 R_m R_p C_m^2)(1 + \omega_c^2 R_p^2 C_m^2)}\right]. \tag{14}$$

The solid line in Fig. 3 *A* indicates the C_m noise predicted using Eq. 14, which agrees quite well with the experimental measurements from the model circuit.

The "extra" noise at low frequencies is accompanied by a correlation of capacitance estimates

In general, averaging N uncorrelated data points results in a N-fold decrease in variance of the averaged data as com-

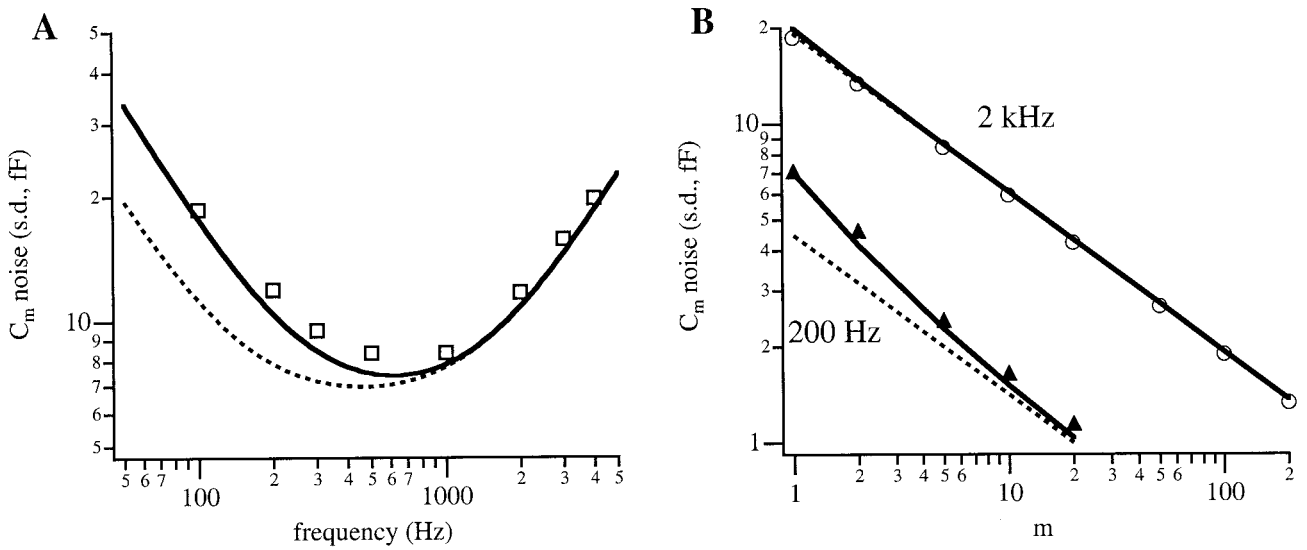

FIGURE 3 The C_m noise of a model circuit can be predicted using Eq. 14. The model circuit (MC-9) had nominal values of $C_m = 22$ pF, $R_A = 5$ MΩ, and $R_m = 0.5$ GΩ. (*A*) The squares indicate the measured C_m noise (standard deviation), whereas the dashed line indicates the theoretical noise from Eq. 12 (Gillis 1995). The solid line is calculated from Eq. 14. Note that the correction factor in Eq. 14 is necessary to describe the noise at low frequencies. The value of m was adjusted so that the noise bandwidth (f_c/m) was always 100 Hz. The amplitude of the sine wave stimulus was 10 mV. (*B*) At low frequencies, increasing m steeply decreases the noise of C_m estimates, which indicates a correlation between estimates. The triangles were obtained for a stimulus of 200 Hz, whereas the circles were obtained for a stimulus of 2 kHz. The dashed lines indicate the expected noise from Eq. 12, whereas the solid lines are from Eq. 14. The amplitude of the sine wave stimulus was 25 mV for these measurements.

pared to the original data (Melsa and Sage, 1973). For the case of capacitance estimation, increasing the number of sine wave cycles that are processed to generate a single estimate (m) lowers the C_m noise, but at the price of lowering the time resolution of estimates, which are generated at a rate of f_c/m. If the capacitance estimates are uncorrelated, then the variance of C_m estimates should be inversely proportional to m (as predicted in Eq. 12). However, Eq. 14 dictates that C_m noise has a steeper dependence on m at low frequencies, which indicates that the C_m estimates are correlated with each other. To confirm this prediction, the noise of capacitance estimates measured from a model circuit is plotted as a function of m in Fig. 3 *B*. Measurements at a low (200 Hz, *triangles*) and a high (2 kHz, *circles*) frequency are plotted as a function of m on a double logarithmic scale in Fig. 3 *B*. The dashed line indicates the noise predicted from Eq. 12, whereas the solid line includes the correction given by Eq. 14. Note that the noise (standard deviation) obtained with a stimulus frequency of 200 Hz decreases more steeply than $m^{-0.5}$ (i.e., estimates are correlated with each other), whereas noise obtained with a stimulus frequency of 2 kHz is closely approximated by Eq. 12.

1/*f*-Like noise increases the variance of C_m estimates at low stimulus frequencies

Whereas Eq. 14 is quite successful in describing the frequency dependence of C_m noise in model circuits, actual whole-cell recordings may have additional sources of current noise. If thermal noise is the dominant noise source, then Eq. 1 predicts that the current spectral density should be linearly proportional to the Real part of the admittance. Figure 4 *A* plots the relationship between S_I and Real$\{Y(f)\}$ for 6 cells measured over the frequency range between 200 Hz and 5 kHz. At high values of Real$\{Y(f)\}$ (corresponding to frequencies ≥1 kHz), the linear relationship holds. However, the current noise is higher than predicted for frequencies less than 1 kHz.

Figure 4 *B* illustrates that the excess noise at low frequencies has a 1/*f*-like characteristic (Benndorf, 1995; Marty and Neher, 1995). The smooth line in Fig. 4 *B* indicates that the measured current power spectral density in the whole-cell mode can be fit by a sum of a 1/*f* component and a thermal noise component,

$$S_I(f) = A/f + 4kT \cdot \text{Real}\{Y(f)\}. \quad (15)$$

1/*f*-Like current noise is not prominent in the on-cell configuration before patch rupture (data not shown). Therefore, the origin of this noise source is inherent in the whole-cell configuration and does not originate from the recording apparatus (e.g., from the pipette holder).

1/*f* Noise, or, more generally, noise with a $1/f^n$ spectrum (hence, 1/*f*-like) is also called "flicker noise," and is encountered in a wide variety of physical measurements. In addition, a myriad of physical processes can produce noise with a 1/*f*-like characteristic (DeFelice, 1981). If a tight seal

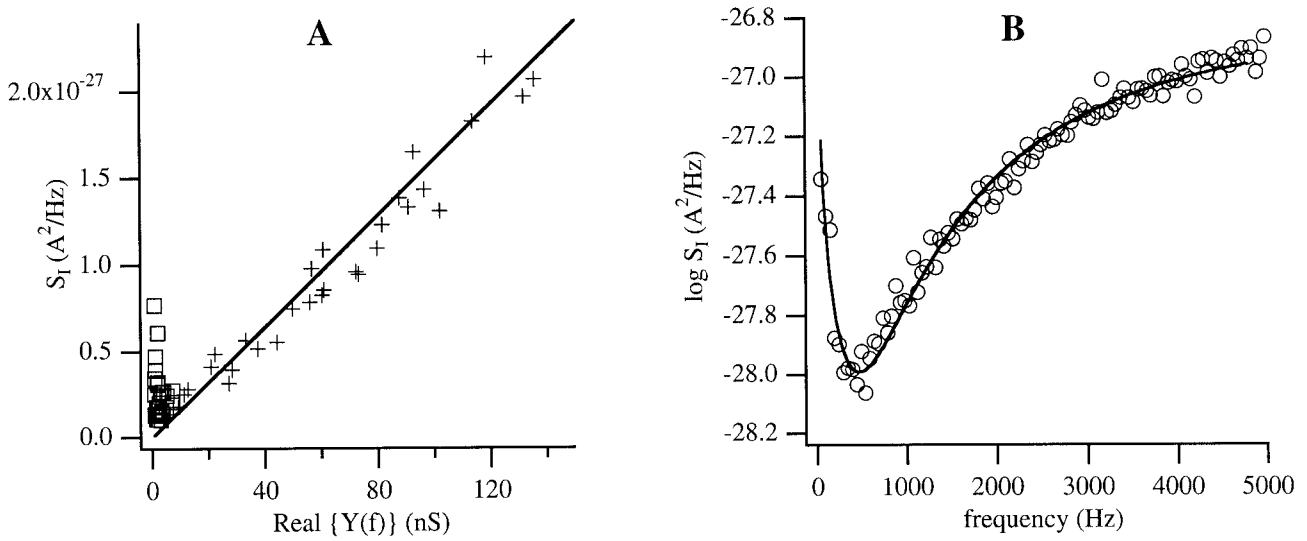

FIGURE 4 1/*f* current noise dominates at low frequencies in whole-cell measurements. (*A*) The current power spectral density is plotted as a function of the measured Real part of the admittance. The solid line indicates the relationship expected for thermal noise ($S_I = 4kT\,\mathrm{Real}\{Y(f)\}$). The crosses indicate values measured from 6 cells (4 chromaffin, 2 NIH-3T3) for frequencies between 1 and 5 kHz. The squares indicate values measured from the same cells between 200 and 500 Hz. The chromaffin cells had the following equivalent circuit parameters (mean ± SD). C_m, 6.2 ± 1.2 pF; R_m, 8.1 ± 1.2 GΩ; R_A, 8.2 ± 2.6 MΩ. The NIH-3T3 cells had the following parameters: C_m, 10.1, 10.6 pF; R_m, 5.3, 2.3 GΩ; R_A, 5.9, 5.6 MΩ. (*B*) Circles indicate the current power spectral density for a typical chromaffin cell held at −70 mV. The line indicates a fit of Eq. 15 to the noise, which resulted in an estimated value of 2.9×10^{-26} A^2 for the amplitude of the 1/*f* component (*A*).

(>10 GΩ) is not obtained, we found that the leakage current contributes a large 1/*f*-like characteristic (data not shown). In contrast, we saw no apparent correlation between values of R_A, R_m, and C_m and the amplitude of the 1/*f* component.

One possible origin of flicker noise in whole-cell recordings is the gating of ion channels (Marty and Neher, 1995). In this case, the amplitude of the 1/*f* component (*A* in Eq. 15) can be expected to be a function of the membrane potential and vary from cell to cell and between different cell types. Indeed, depolarization in a physiological extracellular saline solution increases the value of *A* in chromaffin cells (Marty and Neher, 1995 and data not shown). However, tight-seal recordings from two very different cell types, the excitable chromaffin cell and the nonexcitable fibroblast cell line NIH-3T3, often exhibited a similar value of *A* when the cell is held at −70 mV. Figure 5 *A* plots the *A* value as a function of holding potential for 4 chromaffin cells and 2 NIH-3T3 cells under conditions where voltage-gated K^+, Na^+, and Ca^{2+} channels are blocked. Note that the two very different cell types exhibit similar magnitudes of 1/*f* noise that varies very little with shifts in holding potential. Therefore, the dominant source of 1/*f* noise under common recording conditions (tight seal, hyperpolarized holding potential, little ion channel activity) is cell-type independent and has a typical amplitude of 4×10^{-26} A^2.

Calculation of C_m noise due to 1/*f* current noise

The additional noise of C_m estimates due to the *A*/*f* term in Eq. 15 can be estimated by solving Eq. 6 and applying Eq. 8. Numerical simulations (data not shown) suggest that the approximation of Eq. 10 is appropriate. Therefore, the variance of the admittance estimate due to the 1/*f* component is approximately given by

$$\sigma^2_{\hat{Y},1/f} \approx \frac{1}{U^2} S_I(f_c) B_N = \frac{A}{mU^2}. \tag{16}$$

Application of Eqs. 8 and 9 gives the variance of C_m estimates due to 1/*f* noise,

$$\sigma^2_{\hat{C},1/f} \approx \frac{A(1 + \omega_c^2 R_p^2 C_m^2)^2 R_t^4}{m\omega_c^2 U^2 R_m^4}. \tag{17}$$

The total variance of C_m estimates is then given by the sum of Eqs. 14 and 17.

Figure 5 *B*, *squares*, is a plot of C_m noise as a function of frequency for a typical cell. The solid line indicates the noise predicted from Eqs. 14 and 17, whereas the dashed line neglects 1/*f* noise (i.e., Eq. 14). Note that the 1/*f* noise term dominates for frequencies less than 1 kHz. Figure 6 compares the theoretical and measured C_m noise for 6 cells (4 chromaffin and 2 NIH-3T3) over a frequency range of 200 Hz to 5 kHz. These results demonstrate that Eqs. 14 and 17 can accurately describe C_m noise for whole-cell recordings over a wide frequency range.

Series resistance compensation can reduce C_m noise at high frequencies

Consideration of Eqs. 14, 17, and experimental measurements such as Fig. 5 *B* suggest that the optimal frequency

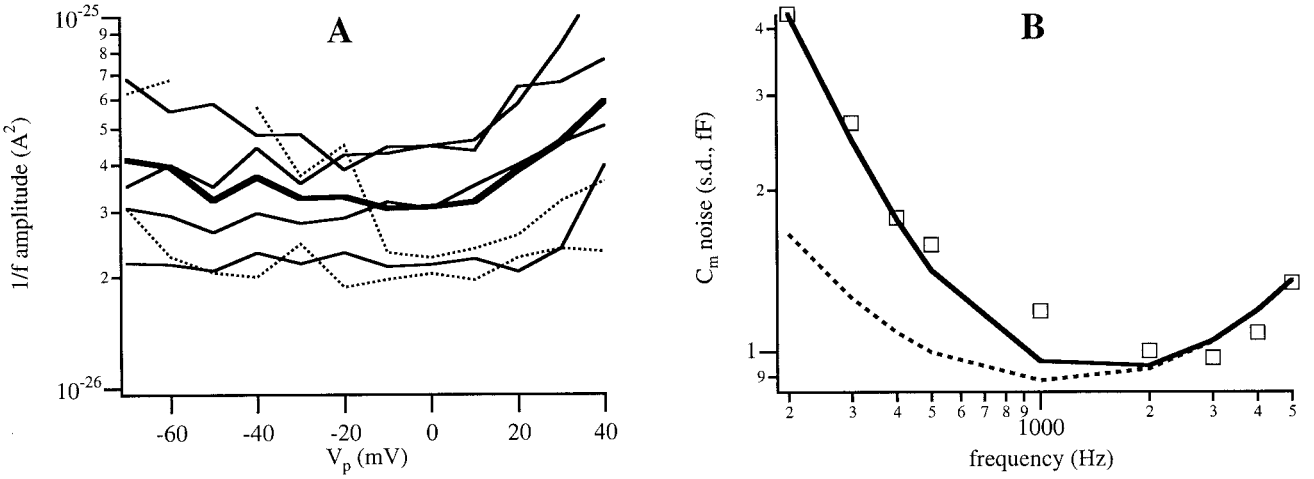

FIGURE 5 (*A*) 1/*f* Noise does not depend on voltage or cell type if voltage-dependent channels are blocked. Voltage-dependent channels were blocked by including 10 μM tetrodotoxin and 50 μM $CdCl_2$ in the bath solution. The amplitude of the 1/*f* component (*A*) was found by fitting Eq. 15 to the current power spectral density and is plotted as a function of the *dc* holding potential (V_p). The solid lines are from 4 chromaffin cells, whereas the dashed lines are from 2 NIH-3T3 cells. The equivalent circuit parameters for the cells are given in the legend to Fig. 4. The dark line indicates the average value. (*B*) 1/*f* Current noise leads to increased C_m noise at low frequencies. The squares indicate measurements from a typical chromaffin cell. The dashed line indicates the predicted noise from Eq. 14 (neglecting 1/*f* noise), and the solid line includes the predicted noise of the 1/*f* component given by Eq. 17.

for whole-cell C_m measurements is higher than previously believed. What noise source dominates at high stimulus frequencies? The main limitation at high frequencies is that, as the impedance of C_m becomes quite low, the stimulus voltage begins to drop across the pipette resistance (R_A) rather than across the membrane. Therefore, the amplitude of the stimulus that drops across C_m (U_{eff}) becomes small for frequencies above $1/(2\pi R_p C_m)$:

$$U_{eff} = \frac{U}{(1 + \omega_c^2 R_p^2 C_m^2)^{1/2}}. \quad (18)$$

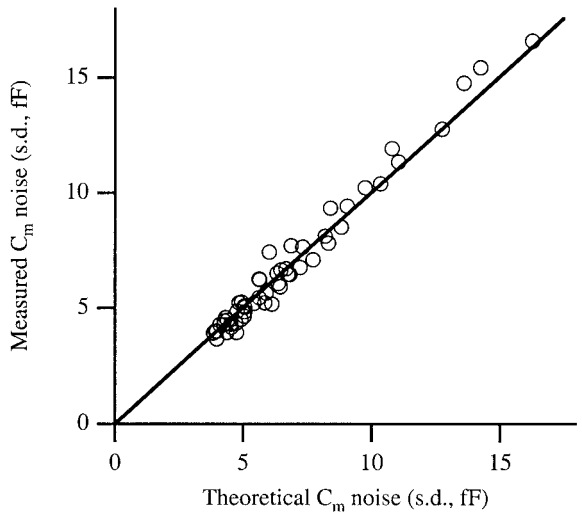

FIGURE 6 The C_m noise of cells in the whole-cell recording configuration can be predicted using Eqs. 14 and 17. The circles indicate theoretical and measured C_m noise from 6 cells (4 chromaffin and 2 NIH-3T3) for stimulus frequencies between 200 Hz and 5 kHz. The solid line has a slope of 1.

Increasing U reduces C_m noise (see Eqs. 14 and 17). However, in practice, U must be limited. In excitable cells, the most positive (depolarizing) excursion of the stimulus must not activate nonlinear, voltage-dependent ion conductances. In nonexcitable cells, U may be somewhat larger. However, too large a value can lead to electroporation of the membrane. Both of these concerns, however, limit the voltage across the membrane (U_{eff}), and not the total voltage applied to the pipette (U). Therefore, in principle, the amplitude of the stimulus sinusoid can be boosted to compensate for the drop across R_A. Compensating for a voltage drop across R_A is a common problem in whole-cell recording and is commonly addressed using series-resistance compensation circuitry of the patch-clamp amplifier. This circuitry adds a scaled version of the measured current ($\alpha R_A i_p$) to the stimulus voltage to partially compensate for the drop of the stimulus voltage across R_A ($= R_A i_p$; Sigworth, 1995). Because this is a form of positive feedback, the system is stable only for partial compensation ($\alpha < 1$). In principle, the same circuitry can decrease C_m noise at high frequencies by automatically boosting the amplitude of the stimulus sinusoid. Figure 7 (*circles*) demonstrates that use of series-resistance compensation circuitry can reduce C_m noise measured from a model circuit. It is important to note, however, that this feedback technique also introduces noise into the stimulus pathway. So, the C_m noise can actually be higher if

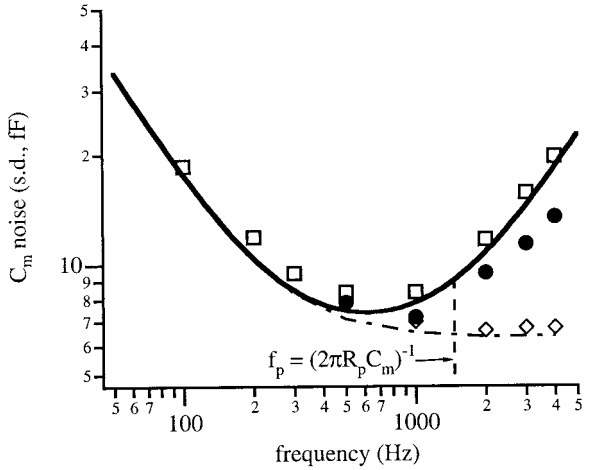

FIGURE 7 The noise of capacitance estimates can be reduced by compensating for the series resistance. The squares and the solid line were taken from Fig. 3 *A* and indicate the noise measurements and theoretical response (Eq. 14) for a model circuit. The filled circles indicate measurements where 50% series resistance compensation in the patch-clamp amplifier is used. The diamonds indicate noise levels measured when the amplitude of the stimulus sinusoid is boosted to compensate for the voltage drop across R_A (see Eq. 18). The dot-dash line indicates the minimum noise expected for this case (Eq. 14).

large compensation values ($\alpha \gtrsim 0.5$) are used (data not shown). A more reliable approach is to have the software boost the amplitude of the stimulus sinusoid by an appropriate amount to compensate for the drop across R_A. Figure 7 (*diamonds*) indicates the noise level achieved when the amplitude of the stimulus sinusoid is boosted to take into account the voltage drop across R_A. A similar hardware-based approach was reported by Rech et al. (1996).

DISCUSSION

Understanding and modeling the dominant noise sources for capacitance measurement in the whole-cell configuration is important for optimizing recording conditions. Reducing the noise of whole-cell capacitance measurements is particularly important when attempting to measure small amounts of evoked exocytosis (e.g., Horrigan and Bookman, 1994; Gillis et al., 1996) or to resolve unitary fusion (exocytic) or fission (endocytic) events (e.g., Chow et al., 1996; Moser and Neher, 1997; Zupancic et al., 1994).

Eqs. 14 and 17 successfully describe the noise of C_m measurements over a wide frequency range in recordings from actual cells (Fig. 6). These results demonstrate that the dominant noise source at high stimulus frequencies is the thermal noise of the equivalent circuit, whereas 1/*f*-like current noise has a large impact on the noise of C_m estimates at low stimulus frequencies. The noise of the patch-clamp amplifier can also be a significant noise source at low stimulus frequencies (Gillis, 1995), but will dominate experimental noise only under conditions where 1/*f* noise is small (such as with model circuits).

The noise of C_m estimates can always be reduced by decreasing the time resolution of the measurement, e.g., by increasing the number of sine wave cycles that are used to generate a single estimate of C_m (m) when using a software lock-in amplifier. In general, the variance of independent estimates is inversely proportional to m (e.g., Eq. 12). Eq. 14 and Fig. 3 *B* demonstrate that, under some circumstances, increasing m can lower the variance of C_m estimates even more steeply than predicted from the inverse law. This further emphasizes the advantages of filtering (or decimating) C_m estimates to obtain lower noise under conditions where temporal resolution can be sacrificed.

In principle, Eqs. 14 and 17 can be solved to select an optimum stimulus frequency for each recording. However, this is not always very practical because all of the relevant parameters vary from cell to cell and also change during the time course of the recording. Nevertheless, these equations can be used to estimate the optimal frequency range for typical recording conditions. For example, for $R_A = 10$ MΩ, $R_m = 3$ GΩ, $C_m = 6$ pF and $A = 4 \times 10^{-26}$ A^2, the optimal frequency is about 1200 Hz. If a membrane conductance is activated leading to a drop in R_m to 100 MΩ and a rise in the 1/*f* amplitude to 2×10^{-25} A^2, then the optimum frequency increases to about 2 kHz. As the desired frequency approaches or exceeds $1/(2\pi R_p C_m)$ (2.9 kHz in this example), then some form of series resistance compensation can be used to reduce C_m noise. In our example, only 82% of the stimulus voltage drops across C_m for a stimulus frequency of 2 kHz (Eq. 18).

Although our analysis has concentrated on estimating C_m using a stimulus containing a single sinusoid, our results have implications for using multiple sinusoids to calculate equivalent circuit parameters. For example, our results suggest that the approach for estimating equivalent circuit parameters developed by Barnett and Misler (1997) should be amended to include the 1/*f* source in the noise model (Eq. 15). In addition, unlike the approach of Barnett and Misler, our noise model does not include the effects of the low-pass filters of the patch-clamp amplifier. We found that low-pass filtering has little effect on C_m noise when these filters are set to an appropriate cutoff value ($\geq 2f_c$, Gillis, 1995), because the overall transfer function (H_{psd}) is dominated by the band-pass characteristic of the phase-sensitive-detector (Fig. 2 and data not shown). Although low-pass filtering may not affect C_m noise, it is important to note that the phase shift and attenuation of the current signal produced by these filters needs to be taken into account to generate C_m estimates based upon admittance measurements (Gillis, 2000).

Finally, it should be noted that the expressions for C_m noise derived in this work do not depend on the exact method that is used to calculate equivalent circuit parame-

ters. The method that was used in this work to measure C_m noise was the sine + dc technique, which has also been called the Lindau–Neher method (Pusch and Neher, 1988; Gillis, 1995; Lindau and Neher, 1988). However, the piecewise-linear technique (Neher and Marty, 1982; Fidler and Fernandez, 1989; Gillis, 1995), which is based upon an approximation similar to that of Eq. 8, has identical C_m noise characteristics (data not shown). Therefore, any optimally implemented technique that uses a single sinusoidal stimulus can be expected to have a minimal variance of C_m estimates described by Eqs. 14 and 17.

APPENDIX

Our goal is to solve Eq. 6 to obtain the variance of the estimate of the real or imaginary component of the admittance ($\sigma^2_{\hat{Y}}$). Because directly solving Eq. 6 is not straightforward, we will use a time-domain approach that is based upon first principals. First, we combine Eqs. 1 and 3 to give the current power spectral density of the equivalent circuit,

$$S_I(f) = 4kT \cdot \text{Real}\{Y(f)\} = 4kT\frac{1 + \omega^2 R_m R_p C_m^2}{R_t(1 + \omega^2 R_p^2 C_m^2)} \quad 0 \le f < \infty. \tag{19}$$

Next, S_I is written in terms of the Laplace variable $s = j\omega$ after partial-fraction expansion,

$$S_I(s = j\omega) = \frac{4kT}{R_A} - \frac{4kTR_m}{R_A R_t}\left(\frac{1}{1 - R_p^2 C_m^2 s^2}\right). \tag{20}$$

An inverse Fourier transformation of the power spectral density yields the auto correlation function of the current (Wiener–Khintchine relationship, Melsa and Sage, 1973),:

$$C_I(\Delta t) = \frac{2kT}{R_A}\delta_D(\Delta t) - \frac{kTR_m}{R_p C_m R_A R_t}\exp[-|\Delta t|/(R_p C_m)] = X_1\delta_D(t_2 - t_1) - X_2 e^{-|t_2 - t_1|/\tau} \quad (-\infty < \Delta t = t_2 - t_1 < \infty), \tag{21}$$

where,

$$\tau = R_p C_m, \quad X_1 \equiv \frac{2kT}{R_A}, \quad \text{and} \quad X_2 \equiv \frac{kTR_m}{\tau R_A R_t}.$$

The current is processed by the phase-sensitive detector according to Eq. 5 to produce estimates of the real and imaginary component of the admittance. We will arbitrarily consider the variance of the real component. Because Eq. 5 is a linear transformation of the current, the expectation operation can be brought inside the integral, resulting in a variance given by

$$\begin{aligned}\sigma^2_{\hat{Y}} &= \frac{4}{U^2(mT_c)^2}\int_0^{mT_c}\int_0^{mT_c} C_I(t_2 - t_1)\cos(\omega_c t_1)\cos(\omega_c t_2)\, dt_1\, dt_2 \\ &= \frac{4}{U^2(mT_c)^2}\int_0^{mT_c}\cos(\omega_c t_2) \\ &\quad \times\left[X_1\cos(\omega_c t_2) - X_2 e^{-t_2/\tau}\int_0^{t_2} e^{t_1/\tau}\cos(\omega_c t_1)\, dt_1 \right. \\ &\quad \left. - X_2 e^{t_2/\tau}\int_{t_2}^{mT_c} e^{-t_1/\tau}\cos(\omega_c t_1)\, dt_1\right] dt_2. \end{aligned} \tag{22}$$

Evaluating the integrals and simplifying,

$$\begin{aligned}\sigma^2_{\hat{Y}} &= \frac{2X_1}{U^2 mT_c} - \frac{4\tau X_2}{U^2 mT_c[1 + (\omega_c\tau)^2]} + \frac{8\tau^2 X_2(1 - e^{-mT_c/\tau})}{U^2(mT_c)^2[1 + (\omega_c\tau)^2]^2} \\ &= \frac{4kT[1 + R_m R_p \omega_c^2 C_m^2]}{U^2 mT_c R_t[1 + (\omega_c\tau)^2]} + \frac{8\tau kTR_m(1 - e^{-mT_c/\tau})}{U^2(mT_c)^2 R_A R_t[1 + (\omega_c\tau)^2]^2} \\ &= \frac{S_I(f_c)}{U^2 mT_c} \times\left[1 + \frac{2f_c R_m^2 C_m(1 - e^{-mT_c/R_p C_m})}{mR_t(1 + \omega_c^2 R_m R_p C_m^2)(1 + \omega_c^2 R_p^2 C_m^2)}\right]. \end{aligned} \tag{23}$$

The term to the left of the braces can be recognized as identical to the approximate expression given by Eqs. 10 and 11 ($\sigma^2_{\hat{Y},approx}$). The term in the braces equals the correction factor of Eq. 13. Finally, the variance of C_m estimates (Eq. 14) is obtained in a straightforward manner using Eqs. 8 and 9.

We would like to thank Yan Jun Wang for preparing chromaffin cells and Dr. David Barnett for critically reading the manuscript. This work was supported by a grant from the Whitaker Foundation to K.D.G.

REFERENCES

Barnett, D. W., and S. Misler. 1997. An optimized approach to membrane capacitance estimation using dual-frequency excitation. *Biophys. J.* 72: 1641–1658.

Benndorf, K. 1995. Low-noise recording. *In* Single-Channel Recording. B. Sakmann and E. Neher, editors. Plenum Press, New York. 129–145.

Chow, R. H., J. Klingauf, C. Heinemann, R. S. Zucker, and E. Neher. 1996. Mechanisms determining the time course of secretion in neuroendocrine cells. *Neuron.* 16:369–376.

DeFelice, L. J. 1981. Introduction to membrane noise. Plenum Press, New York.

Fidler, N., and J. M. Fernandez. 1989. Phase tracking: an improved phase detection technique for cell membrane capacitance measurements. *Biophys. J.* 56:1153–1162.

Gillis, K. D. 1995. Techniques for membrane capacitance measurements. *In* Single-Channel Recording. B. Sakmann and E. Neher, editors. Plenum Press, New York and London. 155–197.

Gillis, K. D. 2000. Admittance-based measurement of membrane capacitance using EPC-9 patch clamp amplifier. *Pflügers Arch.* 439:655–664.

Gillis, K. D., R. Moessner, and E. Neher. 1996. Protein kinase C enhances exocytosis from chromaffin cells by increasing the size of the readily releasable pool of secretory granules. *Neuron.* 16:1209–1220.

Horrigan, F., and R. Bookman. 1994. Releasable pools and the kinetics of exocytosis in adrenal chromaffin cells. *Neuron.* 13:1119–1129.

Lindau, M., and E. Neher. 1988. Patch-clamp techniques for time-resolved capacitance measurements in single cells. *Pflugers Arch.* 411:137–146.

Lollike, K., N. Borregaard, and M. Lindau. 1995. The exocytotic fusion pore of small granules has a conductance similar to an ion channel. *J. Cell Biol.* 129:99–104.

Marty, A., and E. Neher. 1995. Tight-seal whole-cell recording. *In* Single-Channel Recording. B. Sakmann and E. Neher, editors. Plenum Press, New York. 31–52.

Melsa, J. L., and A. P. Sage. 1973. An Introduction to Probability and Stochastic Processes. Prentice-Hall, Englewood Cliffs, NJ.

Moser, T., and E. Neher. 1997. Estimation of mean exocytic vesicle capacitance in mouse adrenal chromaffin cells. *Proc. Natl. Acad. Sci. USA.* 94:6735–6740.

Neher, E., and A. Marty. 1982. Discrete changes of cell membrane capacitance observed under conditions of enhanced secretion in bovine adrenal chromaffin cells. *Proc. Natl. Acad. Sci. USA.* 79:6712–6716.

Pusch, M., and E. Neher. 1988. Rates of diffusional exchange between small cells and a measuring patch pipette. *Pflugers Arch.* 411:204–211.

Rech, F., V. Rohlicek, and A. Schmid. 1996. A method of resolution improvement by the measurement of cell membrane capacitance. *Physiol Res.* 45:421–425.

Sigworth, F. J. 1995. Electronic design of the patch clamp. *In* Single-Channel Recording. B. Sakmann and E. Neher, editors. Plenum Press, New York. 95–127.

Zhou, Z., and E. Neher. 1993. Mobile and immobile calcium buffers in bovine adrenal chromaffin cells. *J. Physiol. (Lond).* 469:245–273.

Zupancic, G., L. Kocmur, P. Veranic, S. Grilc, M. Kordas, and R. Zorec. 1994. The separation of exocytosis from endocytosis in rat melanotroph membrane capacitance records. *J. Physiol. (Lond).* 480:539–552.